

A fresh look at the structure of aromatic thiols on Au surfaces from theory and experiment

Cite as: J. Chem. Phys. 155, 044707 (2021); doi: 10.1063/5.0053493

Submitted: 8 April 2021 • Accepted: 14 July 2021 •

Published Online: 29 July 2021



View Online



Export Citation



CrossMark

Joscha Hekele,^{1,a)} Matthias Linke,² Thomas Keller,² Jesil Jose,² Marvin Hille,²
Eckart Hasselbrink,^{2,b)} Sebastian Schlücker,^{2,c)} and Peter Kratzer^{1,d)}

AFFILIATIONS

¹ Faculty of Physics and Center for Nanointegration (CENIDE), University of Duisburg-Essen, Duisburg, Germany

² Faculty of Chemistry and Center for Nanointegration (CENIDE), University of Duisburg-Essen, Essen, Germany

^{a)} Author to whom correspondence should be addressed: joscha.hekele@uni-due.de

^{b)} Electronic mail: eckart.hasselbrink@uni-due.de

^{c)} Electronic mail: sebastian.schluecker@uni-due.de

^{d)} Electronic mail: peter.kratzer@uni-due.de

ABSTRACT

A detailed study of the adsorption structure of self-assembled monolayers of 4-nitrothiophenol on the Au(111) surface was performed from a theoretical perspective via first-principles density functional theory calculations and experimentally by Raman and vibrational sum frequency spectroscopy (vSFS) with an emphasis on the molecular orientation. Simulations—including an explicit van der Waals (vdW) description—for different adsorbate structures, namely, for $(\sqrt{3} \times \sqrt{3})$, (2×2) , and (3×3) surface unit cells, reveal a significant tilting of the molecules toward the surface with decreasing coverage from 75° down to 32° tilt angle. vSFS suggests a tilt angle of 50° , which agrees well with the one calculated for a structure with a coverage of 0.25. Furthermore, calculated vibrational eigenvectors and spectra allowed us to identify characteristic in-plane (NO_2 scissoring) and out-of-plane (C–H wagging) modes and to predict their strength in the spectrum in dependence of the adsorption geometry. We additionally performed calculations for biphenylthiol and terphenylthiol to assess the impact of multiple aromatic rings and found that vdW interactions are significantly increasing with this number, as evidenced by the absorption energy and the molecule adopting a more upright-standing geometry.

Published under an exclusive license by AIP Publishing. <https://doi.org/10.1063/5.0053493>

I. INTRODUCTION

Long-chain alkylthiol and (oligo-)phenylthiol molecules have been shown to form ordered adsorbate layers on gold surfaces. Scanning tunneling microscopy^{1,2} has revealed that for the latter, the degree of spatial order is highest for densely packed layers of polyaromatic molecules, e.g., molecules with two or more phenyl rings in a row bound to the sulfur anchor atom. The orientation of such molecules with respect to the surface is an interesting question to study since it is governed by coordination chemistry at the sulfur atom linking the molecule to the substrate but also strongly depends on the intermolecular interactions. On one hand, one could hypothesize that the divalent sulfur atom forms two bonds enclosing an angle of 92° as in H_2S or 99° as in $(\text{CH}_3)_2\text{S}$. In these molecules, the S orbitals involved in the bonding display mostly *p* character (and only little *s* character), resulting in a bond angle considerably smaller than the ideal tetrahedral angle of 109.5° known from *sp*³

bonding. On the other hand, if one assumed that the sulfur bonds to the Au surface mainly by getting immersed into the electron liquid of the surface, the S–C bond would not show a directional preference, and the orientation of the molecular chain should be rather free and thus susceptible to other factors (different from the orbital hybridization at the S atom), such as electrostatic or van der Waals (vdW) interactions between the phenyl groups or the nitro group and the surface.

Several experimental methods have been utilized to explore the molecular orientation; however, a conclusive picture is still elusive. In the literature, there is evidence for both, molecules standing upright or with a tilt. Near-edge x-ray absorption fine structure spectroscopy (NEXAFS) has suggested that thiophenol (TP) SAMs on Au are tilted by about 50° with respect to the surface normal.³ In contrast, the results from electron spectroscopy have been interpreted as evidence for flat-lying TP SAMs on the Au surfaces.⁴ Another piece of evidence comes from the work of Tao

et al. who analyzed the orientation of aromatic-derivatized SAMs through reflection absorption infrared spectroscopy (RAIRS, a technique that is admittedly not precise for this purpose) and observed that they are preferentially inclined toward the Au surface.⁵ This is in contrast to work supporting a nearly upright molecular orientation, e.g., by McNally *et al.*⁶ who employed RAIRS and ellipsometry. Moreover, Wan *et al.*⁷ reported a tilt angle of about 30° based on surface-enhanced infrared absorption spectroscopy (SEIRAS) measurements. Carron and Hurley⁸ reported a tilt angle of about 14°, measured by surface-enhanced Raman scattering (SERS).

In this paper, we attempt to resolve the issue of lying vs standing by studying 4-nitrothiophenol (4-NTP) and its biphenyl and terphenyl variants on Au. To this end, we carry out first-principles calculations for periodic slab models of the Au(111) surface that allow us to address the role of intermolecular interactions and of the coverage on the tilt angle. These results are then compared for the simplest molecule with just one phenyl ring (4-NTP) to experimental evidence. In a first exploration, we employ Raman spectroscopy to detect the vibrational signature of this molecule adsorbed on the Au(111) face. We expect to observe the out-of-plane modes if molecules were lying flat, whereas in-plane modes should be strongly enhanced in the case of an upright orientation. In the experiment, we observe the presence of out-of-plane modes in the vibrational Raman spectra, pointing to a tilted orientation of 4-NTPs on the Au surface. Eventually, we exploit the polarization dependence of vibrational sum frequency spectroscopy (vSFS), specifically the symmetric stretch mode of the NO₂ group, to gather orientational information. This highly sensitive method had been applied before to 4-NTP on Au.^{9,10} In previous work,⁹ evaluation of the polarization dependence of SF signals suggested an inclination of the molecular symmetry axis by 60° with respect to the surface normal, while our present analysis yields 50°. This difference may stem from different coverages of the Au(111) surface obtained in these experiments. This is consistent with quite different values reported for the coverage in TP SAMs on Au(111) in the literature, e.g., 0.23 and 0.31⁷ or 0.45.¹¹ Unfortunately, theoretical interpretation of the data, e.g., in Ref. 12, has so far relied on cluster models of the surface with a single molecule adsorbed. A systematic theoretical study of the effects of finite surface coverage and intermolecular interaction effects has so far only been carried out for alkylthiol SAMs^{13,14} and is lacking for TP SAMs. The present study that puts emphasis on the theoretical modeling of SAMs from thiol molecules with a variable number of phenyl rings and at various coverages attempts to fill this gap.

II. METHODS

A. Calculations

The FHI-aims code package,¹⁵ a highly efficient, fully parallelized, numeric atom-centered basis function all-electron code, is used to carry out density functional theory (DFT) calculations. For our calculations, we use the Perdew–Burke–Ernzerhof (PBE) exchange–correlation functional¹⁶ in combination with a “tight” basis set, which is expected to yield well-converged results.¹⁵ The van der Waals (vdW) interactions are described by pairwise potentials using the scheme of Tkatchenko and Scheffler,¹⁷ which employs Hirshfeld partitioning of the electron density to get density-dependent

C_6 coefficients and vdW interaction radii with minimal empirical input. Appropriate correction terms are added to energy and forces after each self-consistency cycle. The geometrical parameters and vibrational frequencies quoted later have been obtained with this method. For additional test calculations of the adsorption energies, we employ two many-body dispersion (MBD) methods,^{18,19} offering an even more sophisticated description of vdW interactions by modeling the response via quantum harmonic oscillators, which are coupled via dynamic dipole interactions. To be specific, we used the range-separated self-consistently screened version (rsSCS-MBD)²⁰ and the more recent non-local version (MBD-NL),²¹ which are both included via the Libmbd library.²² We note that both the Tkatchenko–Scheffler and the MBD method of describing vdW interactions between organic molecules and coinage metal surfaces have been successfully applied to the adsorption of oligo-acenes.^{23–25}

The calculated lattice constants of bulk Au for PBE and PBE + vdW were $a_0 = 4.151$ Å for PBE and $a_0 = 4.108$ Å for PBE + vdW, the latter being very close to the experimental value of 4.080 Å.²⁶ The slab calculations were performed with a $12 \times 12 \times 1$ k-point grid while having a unit cell size of at minimum 100 Å in the z-direction to disable any spurious interactions between slabs. The Au slab was formed by four layers. To compensate for any long-range effects due to the adsorbate-induced polarization, dipole correction²⁷ was applied. Geometry relaxations were generally carried out with a force convergence criterion of 10^{-4} eV/Å, which is a rather tight choice. Relativistic treatment was included via the scaled zeroth order regular approximation (ZORA),²⁸ which uses self-consistent eigenvalues by first constructing the Hamiltonian with an approximate scalar-relativistic kinetic energy operator.

For the calculation of vibrational modes (within the harmonic approximation), we used a python script, which is included in the FHI-aims code package. Here, the Hessian matrix is constructed (and subsequently diagonalized) from force derivatives obtained by a sequence of finite-difference calculations with respect to atomic displacements.²⁹ The same reference holds for the calculation of Raman intensities as presented in Sec. III C, while the required polarizability derivatives were calculated (via finite differences as above) by the density functional perturbation theory (DFPT) functionality,³⁰ which is included in FHI-aims.

B. Sum frequency spectroscopy

For the vibrational sum frequency spectroscopy (vSFS), a Nd:YAG laser (Ekspla PL2231, bandwidth 2 cm^{-1}) pumping a tunable IR OPA/DFG setup (Ekspla PG501DFG, bandwidth 9 cm^{-1}) was used that delivered pulses of 25 ps duration at a repetition rate of 25 Hz, while its frequency doubled fundamental provided the upconversion pulse. Typical pulse energies used were 280 μJ (532 nm) and 10–30 μJ (IR). Both beams were linearly polarized, and a tunable $\lambda/2$ retarding plate (Alphas, PO-TWP-L2-12-IR) was used to control the IR polarization. The IR and upconversion light beams were directed at the sample under incident angles of 43° and 53.5°, respectively. The SF signal was detected using a photomultiplier tube with gated electronics after spectral and spatial filtering. Spectra were obtained by scanning the IR source in 5 nm steps. For every data point, typically 300 shots were sampled and averaged. Self-assembled monolayers of 4-NTP (Tokyo Chemical

Industry Co.) were prepared on thin film Au substrates [13 nm Au on glass slides with a 13 nm titanium adhesion layer in between by placing the substrate for 24 h in a solution in ethanol (PA grade) of about three times the quantity needed for completely covering the surface, typically 70 mg in 100 ml].

C. Raman sample preparation

The Raman measurements on free molecules were performed on a saturated solution of 4-NTP in chloroform in a 1 mm quartz cuvette. Au(111) single crystals were purchased from Surface Preparation Laboratory (Zaandam, The Netherlands) for Raman studies of 4-NTP adsorbed on Au and were used without further surface preparation. The Au(111) single crystals were incubated for 24 h using 4-NTP dissolved in ethanol at two different concentrations (5 and 1 mM) and washed afterward to remove excess 4-NTP.

D. Raman instrumentation

The experiments were performed using a home built confocal Raman microscope comprising an inverted microscope (Nikon Eclipse Ti-S) equipped with a grating spectrometer (HORIBA iHR550, 600 grooves/mm grating) and a back-illuminated CCD camera (HORIBA Synapse). The 632.8 nm radiation from an He-Ne laser was focused onto the sample using a 20 \times microscope objective (Nikon, NA 0.4) for cuvette experiments and using a 60 \times microscope objective (Nikon, NA 0.8) for experiments on molecular adsorbates on Au(111). The experimental parameters are as follows: 15.5 mW laser power at the sample, 2 s integration time, 5 accumulations for cuvette experiments and 10 s integration, and 5 accumulations for measurements on Au(111).

III. RESULTS

A. DFT calculations

Calculations were performed for different coverages of 4-NTP on the Au(111) surface by applying periodic boundary conditions for differently sized surface unit cells. We also aim to assess the impact of the 4-NTP chain length onto structural properties of the SAMs, especially to analyze the role of the intermolecular dispersive interaction. For this purpose, all calculations were also carried out with 4-nitro-biphenyl-4'-thiol (4-NBPT) and 4-nitro-terphenyl-4''-thiol (4-NTPT). Geometry relaxations were then conducted on these setups to retrieve the corresponding equilibrium geometries to be analyzed further. For the slab, different surface coverages were simulated by setting up differently sized unit cells, namely, ($\sqrt{3} \times \sqrt{3}$), (2×2), and (3×3), where the initial location of the 4-NTP molecule was at a hollow position with $\theta = 0^\circ$ and the projection of the phenyl ring normal into the x-y-plane spanning an angle of 30° with the $[1\bar{1}0]$ direction (see Fig. 1 for the specified angles). The initial orientation of the phenyl ring normal reflects the relative orientation of nearest neighbor phenyl ring normals to be on a line in the ($\sqrt{3} \times \sqrt{3}$) system.

1. Optimized geometries

We characterize the orientation of the adsorbed 4-NTP molecule by the tilt angle θ between the molecular axis connecting the sulfur and nitrogen atoms, \mathbf{X}_{S-N} , and the normal of the Au(111) surface. We additionally introduce the sulfur bond tilt

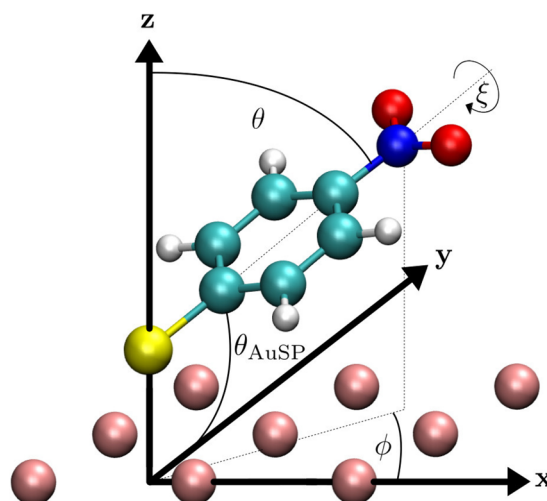


FIG. 1. Bond angle θ_{AuSP} , tilt angle θ of the molecular axis relative to the surface normal, in-plane angle ϕ , measured relative to the $[1\bar{1}0]$ crystallographic direction, and twist angle ξ indicating the rotation of the S-bound phenyl ring around the molecular axis, defined as $\xi = 0^\circ$ when the ring normal is parallel to the surface normal. The line connecting the S and N atoms defines the molecular axis and thus θ and ϕ .

angle θ_{AuSP} , which is calculated from the surface normal and the vector \mathbf{X}_{S-C_1} . Together with the distance between the sulfur atom and the Au(111) surface, $d_{S-\text{Au}}$, it provides information about the sulfur chemical bonds. For a planar molecule, one would expect $\theta_{\text{AuSP}} = 180^\circ - \theta$, but deviations are found due to distortions of the adsorbed molecules away from planarity. Other geometrical parameters of interest are the angle ϕ between the projection of \mathbf{X}_{S-N} into the surface plane and the $[1\bar{1}0]$ crystallographic direction along the x-axis, and the ring twist angle ξ between the surface normal and the phenyl ring normal (see Fig. 1 for a depiction).

Table I shows the data obtained from the final relaxed geometries for the different setups. Relaxed geometries for 4-NTP on the ($\sqrt{3} \times \sqrt{3}$) and the (2×2) surfaces are shown in Fig. 2; in addition, the relaxed structures for both 4-NBPT and 4-NTPT on the (3×3) surface are presented in Fig. 3. If not stated otherwise, we only discuss results here that stem from simulations including vdW interactions as defined above. The vdW, rsSCS-MBD, and MBD-NL methods yield almost the same relaxed geometries with deviations below 1%–2%, as measured by the defined metrics. We therefore do not further discuss these methods for geometry relaxations. Table I shows the relevant data for our following analysis (additional characterization of relaxed geometries can be found in the supplementary material).

We start by discussing the behavior of the sulfur bond angle θ_{AuSP} in dependence of the surface coverage. The calculations suggest that θ_{AuSP} is strongly affected by steric repulsion between the molecules. This is indicated by the angle θ_{AuSP} increasing from 108° to 122° when increasing the coverage from 1/9 [for the (3×3) surface] to 1/4 [for the (2×2) surface]. At the highest coverage of 1/3 [in the ($\sqrt{3} \times \sqrt{3}$) surface], the molecules repel each other and consequently stand almost upright on the surface to make best use of

TABLE I. Calculated values of the bond angle θ_{AuSP} , tilt angle θ , in-plane angle ϕ , twist angle ξ , distance between the Au(111) surface and sulfur and adsorption position of sulfur. The angles are as defined in Fig. 1. All values are from simulations including the Tkatchenko–Scheffler vdW interaction.

Geometry	Rings	θ_{AuSP} ($^\circ$)	θ ($^\circ$)	ϕ ($^\circ$)	ξ ($^\circ$)	$d_{\text{S-Au}}$ (\AA)	Position
$(\sqrt{3} \times \sqrt{3})$	1	136	32.4	29.9	1.5	2.01	Near bridge
	2	149	24.8	307.5	103.7	1.99	Near bridge
	3	151	22.2	113.9	105.0	1.98	Near bridge
(2×2)	1	123	52.8	14.2	4.6	2.05	Bridge
	2	122	50.1	13.5	7.8	2.05	Near bridge
	3	122	48.3	21.0	8.1	2.05	Bridge
(3×3)	1	111	75.7	30.0	2.3	2.14	Bridge
	2	110	71.9	19.8	8.1	2.13	Bridge
	3	108	70.7	13.7	1.2	2.12	Bridge

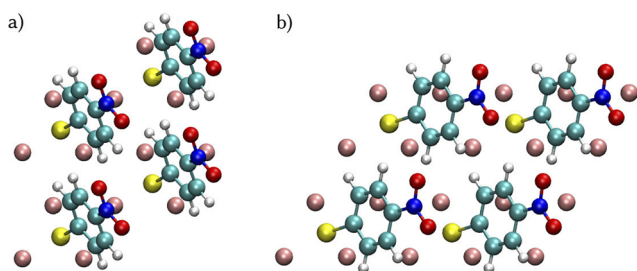
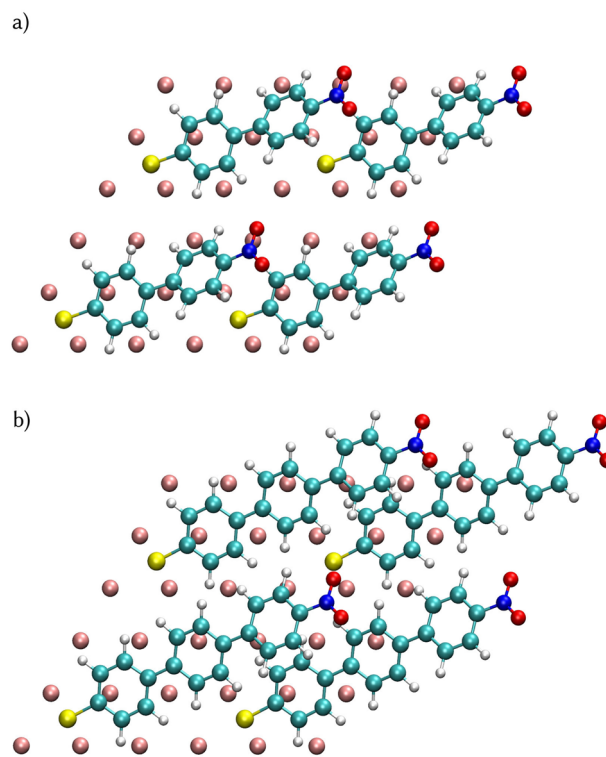
the limited space. This trend is observed for both short- and long-chain molecules, independent of the number of phenyl rings in the molecules. The precise value of the angle θ_{AuSP} , however, is found to depend on the number of phenyl rings, being smallest for 4-NTP and largest for 4-NTPT. Again, this seems to indicate that the repulsion is the dominant interaction, and longer molecular chains are required to stand upright in order to use the limited space on the surface most effectively.

The tilt angle θ of the molecule as a whole shows the same trend as θ_{AuSP} but is more sensitive to the number of rings. Again, small coverage and short-chain molecules favor a geometry in which the molecules lay down on the surface, while large coverage and long-chain molecules favor standing upright. The latter dependence on the chain length is in accord with results from angle-resolved near-edge x-ray absorption fine structure spectroscopy.³ It should be noted that the tilt angle θ is strongly dependent on the inclusion of vdW interactions: If neglected, smaller values are obtained.

The angle ϕ for the relatively isolated molecules (coverage 1/9) is in the range of 20° – 30° . This seems to indicate that the tilting direction is determined by the crystallography of the Au(111) surface; in other words, the molecular axis tilts toward the $[1\bar{1}0]$ azimuth of Au(111). At the coverage of 1/4, ϕ is in the range of 13° – 21° , which allows for a closer alignment of the NO_2 groups of neighboring rows of molecules. Finally, for the most densely packed

layers, the intermolecular interaction becomes more important and ϕ appears to be decoupled from the crystallographic orientation of the surface.

The bond distance of sulfur to the plane of surface Au atoms, $d_{\text{S-Au}}$, is shortest for the densely packed layers and amounts to

**FIG. 2.** Top views of relaxed surfaces for the (a) $(\sqrt{3} \times \sqrt{3})$ and the (b) (2×2) systems incorporating four unit cells, respectively, and only the top Au layer.**FIG. 3.** Top views of relaxed (3×3) surfaces with four unit cells each for (a) 4-NBPT and (b) 4-NTPT, only including the top Au layer. Note the visible internal phenyl ring rotation of 33° for the 4-NBPT. For the 4-NTPT molecules, the first two rings are nearly planar, while the third ring is out of plane by around 20° rotational angle.

2.00 ± 0.02 Å. The increasing tilt angle at higher coverages is found to correlate with a slightly elongated S–Au bond, reaching 2.05 Å at 1/4 coverage and about 2.13 Å at 1/9 coverage. We rationalize these observations in the following way: The more the molecules come close to a flat-lying geometry, the more it matters to have all C atoms of the phenyl ring(s) at a nearly equal, close-to-optimum distance from the surface in order to maximize the vdW attraction. To achieve this energetic goal, it is acceptable to pay the cost of a slightly elongated S–Au bond in order to benefit from the enhanced attractive vdW interactions between Au and the C atoms in the rings. This interpretation is corroborated by observing that, for the most strongly tilted molecules, the lengthening of the S–Au bond is most pronounced for 4-NTPT, where there is the most to be gained from the vdW interaction of three rings with the Au surface.

2. Adsorption energy

The adsorption energies ΔE_{ads} for the fully relaxed geometries are calculated as

$$\Delta E_{\text{ads}} = E_{\text{Au}+4\text{NTP}}^{\text{UC}} + \frac{1}{2}E_{\text{H}_2} - (E_{4\text{NTP}+\text{H}} + E_{\text{Au}}^{\text{UC}}), \quad (1)$$

with $E_{\text{Au}+4\text{NTP}}^{\text{UC}}$ being the total energy of the Au unit cell with adsorbed 4-NTP, E_{H_2} being the total energy of the H_2 molecule, $E_{4\text{NTP}+\text{H}}$ being the total energy of the 4-NTP molecule with hydrogen bonded to sulfur, and $E_{\text{Au}}^{\text{UC}}$ being the total energy in the Au slab unit cell solely (all components are calculated with the same basis set, XC functional, and vdW method, if applicable).

The results are shown in Fig. 4 (numerical data can be found in the [supplementary material](#)). The adsorption energy $|\Delta E_{\text{ads}}|$ increases significantly with the number of rings. The vdW, rsSCS-MBD, and MBD-NL methods yield adsorption energies that essentially only differ by constant shifts. The Tkatchenko–Scheffler method gives the strongest adsorption (ΔE_{ads} is strongly negative), and the non-local MBD method indicates somewhat weaker

adsorption, where both methods differ by around 0.3 eV for one ring, around 0.5 eV for two rings, and around 0.6 eV for three rings, while the rsSCS-MBD method's energies are in between with a slight trend toward MBD-NL energies. For all molecules considered, a major contribution to the adsorption energy comes from the vdW interaction, both with the surface and/or with neighboring molecules. When disregarding any vdW correction, 4-NTP would be unbound, i.e., it shows positive ΔE_{ads} . Only for 4-NBPT and 4-NTPT, there is an adsorption minimum for the lowest coverage of 1/9, which, however, disappears as the coverage is increased.

There is a general tendency for the isolated molecules, in the largest (3×3) supercell, to be most strongly adsorbed, while the repulsion in the denser structures results in a lowering of the adsorption energy. To gain a better understanding of the interaction between the molecules and the surface in the fully relaxed, tilted geometry, a Mulliken charge analysis has been performed. The results discussed here refer to simulations including Tkatchenko–Scheffler vdW interactions. Based on the Mulliken charges and the geometrical data, dipole moments of a corresponding point charge model are calculated, and the results are reported in Table II. The overall charge on the molecules is found to be negative, indicating the transfer of (fractional) electrons from the surface onto the molecule. This charge transfer is strongest for the densely packed layer, where it becomes almost independent of the chain length. This behavior can be rationalized by realizing that the ordered array of molecules builds up a static dipole layer. The concerted effect of the molecular dipoles helps us to pull electronic charge out of the surface onto the molecules. For the lower coverages, the dipole layer becomes weaker due to the sparsity of the molecules, and less charge is accumulated. Eventually, for the smallest coverage, the chain length becomes increasingly important; now, the dipole moment of the molecule as a whole is getting limited by the chain length. A more detailed analysis shows that the largest part of the negative charge pulled onto the molecules is located at the S atom bound to Au, followed by the electronegative oxygen atoms in the NO_2 group. The nitrogen atoms, as well as the outermost phenyl ring, carry positive partial charges. It is remarkable that the net charge on the NO_2 group clearly depends on the surface coverage and is largest for the tilted geometries at small coverage. This indicates that the NO_2 group interacts electrostatically with the Au surface; bringing the NO_2 group closer to the surface by a tilt of the molecule enhances the electrostatic interaction between the NO_2 group and its image charge. Simultaneously, the dipole moment of the NO_2 group increases by roughly a factor of two when going from the densely packed film with upright molecules to the almost isolated tilted molecules in the (3×3) supercell. Again, this indicates that dipolar polarization is built up by the NO_2 group coming closer to the surface and interacting electrostatically with the metal. Moreover, the dipole moment of the NO_2 group also varies strongly with the number of phenyl rings in the molecules, with the larger molecules displaying a larger dipole. To explain this observation, we note that the electronegative oxygen atoms receive electrons donated from the π -orbitals in the aromatic ring system, and 4-NBPT and 4-NTPT appear to be more polarizable and more efficient donors of charge.

Thus, we conclude that the adsorption energy of the thiophenols is governed by a complex interplay of the adsorption geometry and the electrostatic and dispersive interactions enabled by the

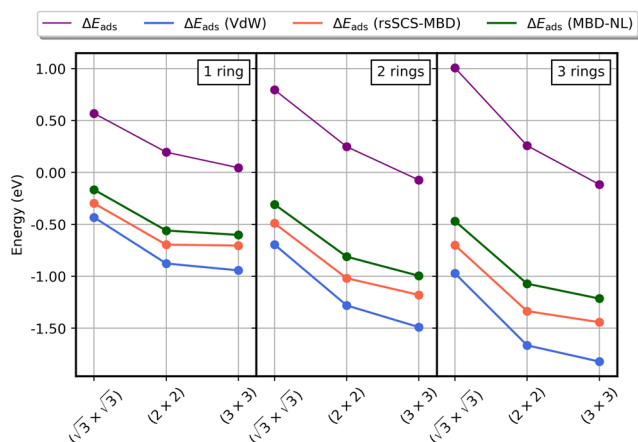


FIG. 4. Adsorption energies, calculated from total energy differences as obtained in the PBE calculations, for the optimized geometries, according to Eq. (1): PBE only (purple), PBE + vdW/Tkatchenko-Scheffler (blue), PBE + rsSCS-MBD (red), and PBE + MBD-NL (green). The lower values indicate energetically more favorable configurations.

TABLE II. Absolute dipole moments generated from Mulliken charges for 4-NTP, 4-NBPT, and 4-NTPT where $\mu_{\text{tot}}^{\text{Mulliken}}$ incorporates the whole respective molecule and $\mu_{\text{NO}_2}^{\text{Mulliken}}$ only incorporates the NO_2 group located at the C(4) atom of the outmost phenyl ring. $q_{\text{tot}}^{\text{Mulliken}}$ and $q_{\text{NO}_2}^{\text{Mulliken}}$ denote the total Mulliken charge of the whole 4-NTP/4-NBPT/4-NTPT molecule and only the NO_2 group, respectively. Results for simulations including Tkatchenko–Scheffler vdW interactions.

Geometry	Rings	$ \mu_{\text{tot}}^{\text{Mulliken}} $ (eÅ)	$ \mu_{\text{NO}_2}^{\text{Mulliken}} $ (eÅ)	$q_{\text{tot}}^{\text{Mulliken}}$ (e)	$q_{\text{NO}_2}^{\text{Mulliken}}$ (e)
$(\sqrt{3} \times \sqrt{3})$	1	0.421	0.964	-0.133	-0.100
	2	0.354	1.599	-0.1325	-0.111
	3	0.364	1.993	-0.138	-0.106
(2×2)	1	0.417	1.707	-0.082	-0.159
	2	0.370	2.383	-0.073	-0.158
	3	0.355	3.054	-0.071	-0.157
(3×3)	1	0.372	2.028	-0.026	-0.193
	2	0.269	3.093	0.059	-0.209
	3	0.189	3.906	0.034	-0.202

geometrical structure. In the densely packed films, an electrostatic dipole along the molecular axis is built up. If the molecules in the less dense films are allowed to relax, their tilting toward the surface enhances both the electrostatic and vdW interactions with the surface. Taking into account the self-consistently built up charge distribution, these interactions stabilize the molecules at some intermediate tilt angle that is limited by the steric repulsion between neighboring molecules. This observation remains qualitatively correct even if different approximate descriptions of the vdW interaction are employed. In all cases, there is only a single covalent bond between the molecule and the surface involved. Even so, the interplay of geometrical relaxation and molecule–surface interaction results in an adsorption energy that varies considerably both with the surface coverage and the molecular chain length.

B. Raman spectroscopy

Figure 5 (top) depicts the normalized experimental Raman spectrum of a saturated 4-NTP solution in chloroform after subtraction of the solvent peaks. The spectrum is dominated by three Raman bands at 1101, 1341, and 1579 cm^{-1} , which are assigned to the phenyl ring C–C stretching, the symmetric NO_2 stretching, and the phenyl ring C=C stretching vibrations, respectively. Less dominant peaks can be observed at 525, 724, 852, and 1078 cm^{-1} , which are assigned to the NO_2 rocking, phenyl ring deformation, NO_2 scissoring, and C–S stretching vibration, respectively. The dip at $\sim 663 \text{ cm}^{-1}$ is due to the subtraction of the intense Raman peak from the solvent chloroform at this position. Figure 5 (middle) depicts the Raman spectrum of 4-NTP adsorbed on the Au(111) single crystal after incubation in a 5 mM solution in ethanol for 24 h. Essentially the same peaks are dominant as in the Raman spectrum of the solvated molecule. In addition, vibrational modes are observed, which were absent in the latter case (740, 1145, 1447 cm^{-1}). The signal from the C–S stretching mode at $\sim 1080 \text{ cm}^{-1}$ is strongly enhanced in the spectrum due to the increased polarizability of the C–S bond due to electron transfer from the Au surface atoms to the S one³¹ confirming the binding of the molecules to the Au(111) surface. The inset shows a magnified view of the region from 400 to 900 cm^{-1} . The

peaks at 528, 721, and 855 cm^{-1} are all due to in-plane (*ip*) vibrations. In addition to these *ip* modes, we observe vibrational modes at 407 cm^{-1} and at 465 cm^{-1} , which we assign to the out-of-plane C–H wagging mode of the phenyl ring. Our calculations (see below) predict a notable variation of vibrational wavenumbers with the coverage of the molecules on the Au(111) substrate. In the case of the

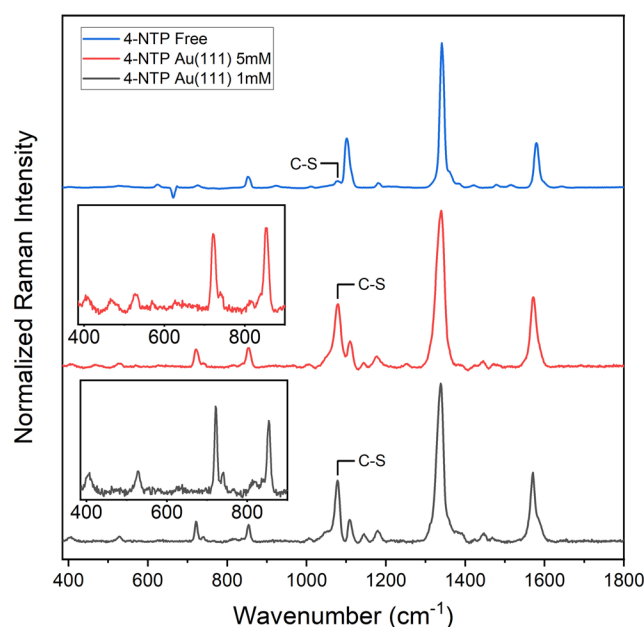


FIG. 5. Top: Normalized Raman spectrum of a saturated 4-NTP solution in chloroform (solvent spectrum subtracted). Middle: Normalized Raman spectrum of 4-NTP adsorbed on Au(111) incubated in a 5 mM solution. The inset shows a zoom into the 400–900 cm^{-1} region. The peaks at 407 cm^{-1} and 465 cm^{-1} are assigned to out-of-plane C–H wagging. Bottom: Normalized Raman spectrum of 4-NTP adsorbed on Au(111) incubated in a 1 mM solution. The peak at 407 cm^{-1} is assigned to out-of-plane C–H wagging.

TABLE III. Selected vibrational modes from DFT calculations within the harmonic approximation for different 4-NTP setups, all relaxed at the same level of theory.

Vibrational frequencies of various modes in different adsorption models (cm^{-1})						
Mode	Free	Au ₇	Au ₁₉	$\sqrt{3} \times \sqrt{3}$	2×2	3×3
C-H wagging	403.5	400.1	401.1	462.8	411.3	403.4
NO ₂ rocking	516.5	516.0	516.4	517.8	527.2	516.2
Ring deformation	719.9	712.8	711.1	714.8	716.2	704.4
Out-of-plane bending	738.4	740.0	735.4	742.1	735.1	734.0
NO ₂ scissoring	840.0	838.9	838.1	843.3	842.4	832.0
C-S	...	1058.1	1052.0	1063.6	1060.0	1039.0
C-C	1084.8	1081.8	1082.6	1084.7	1095.5	1076.9
NO ₂ stretch	1302.3	1301.2	1296.1	1313.3	1305.6	1267.2
C=C	1579.2	1568.1	1564.5	1573.5	1571.1	1551.0

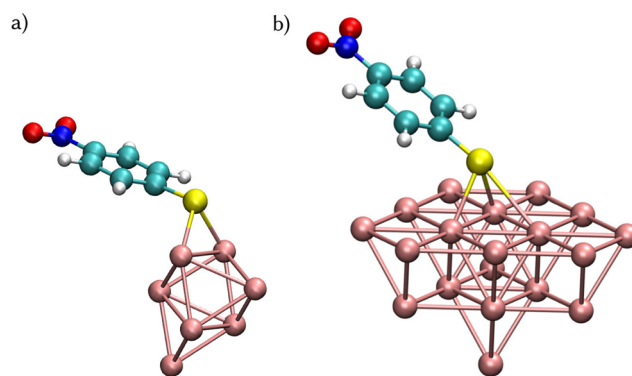
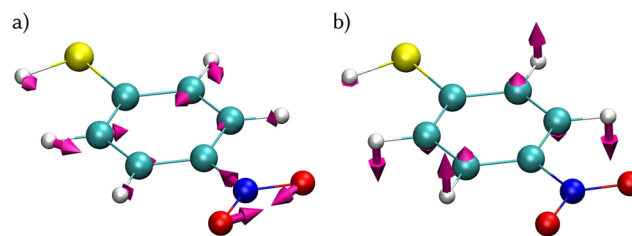
phenyl ring C-H wagging mode, a significant shift from 403 cm^{-1} for free 4-NTP molecules and low coverage (3×3) structure to 462 cm^{-1} in the dense layer with a ($\sqrt{3} \times \sqrt{3}$) structure is expected (cf. Table III). The presence of vibrational modes at both 407 and 465 cm^{-1} points to the coexistence of 4-NTP molecules, which are strongly inclined toward the Au surface (407 cm^{-1}) and standing nearly upright (465 cm^{-1}). This interpretation is consistent with the observation of two kinds of domains, namely, molecules in a well-ordered structure and a disordered phase, of about 10 nm size and equal abundance in an STM study by Nielsen *et al.*³² It cannot be resolved by the optical methods used here probing a focal area larger than $1 \mu\text{m}$.

Figure 5 (bottom) represents the Raman spectrum of 4-NTP molecules adsorbed on Au(111) after incubation in a 1 mM solution in ethanol for 24 h . An enhanced C-S stretching mode at 1078 cm^{-1} again confirms the adsorption of the molecules from the lower concentration solution. The other dominant spectral features remain the same as in the previous cases. The inset gives a magnified view of the $400\text{--}900 \text{ cm}^{-1}$ region, showing the presence of (*ip*) modes at 528 , 721 , and 853 cm^{-1} . Another important spectral feature to be noted is the presence of the peak at 740 cm^{-1} , which is assigned to the anti-symmetric out-of-plane bending of the phenyl ring. The most significant difference between the 1 and the 5 mM spectra is that the vibrational mode at 465 cm^{-1} is absent in the former. This observation combined with the presence of the vibrational modes at 407 and 740 cm^{-1} indicates a situation where the 4-NTP molecules are predominantly tilted toward the Au surface.

Calculated vibrational wavenumbers for both the free molecule and the adsorbed one in various adsorption models are compiled in Table III. In addition to the various slab geometries, we constructed and relaxed two geometries where 4-NTP is bonded to a Au₇ or a Au₁₉ cluster, as illustrated in Fig. 6. The calculations were performed within density functional theory using the PBE functional including vdW interactions in the same manner as before.

Concerning frequency shifts upon adsorption, we find that both cluster models, the Au₇ and the Au₁₉ cluster, give very similar results. Calculations suggest that intermolecular interactions could have an effect on the vibrational frequencies in dense layers. One particular example is the C-H wagging mode of the phenyl ring that is considerably shifted to higher wavenumbers in the dense

layer with a ($\sqrt{3} \times \sqrt{3}$) structure. Moreover, normal mode vectors obtained from the calculations are helpful in the analysis. As an example, calculated displacement vectors of the *ip* NO₂ scissoring C-N vibration and out-of-plane (*oop*) vibration such as the C-H wagging observed in the experimental spectrum at 853 and 407 cm^{-1} , respectively, are displayed in Fig. 7(a).

**FIG. 6.** Setups for 4-NTP bonded to differently sized Au clusters used for vibrational analysis. (a) Au₇ cluster. (b) Au₁₉ cluster.**FIG. 7.** Top and side views of the calculated displacement vectors of (a) the in-plane NO₂ scissoring at 840 cm^{-1} (in the experimental spectrum at 853 cm^{-1}) and (b) the out-of-plane C-H wagging at $\sim 403 \text{ cm}^{-1}$ (in the experimental spectrum at 407 cm^{-1}).

In the slab calculations for various coverages, the build-up of a dipolar field due to the molecular layer is taken into account self-consistently. This leads to a notable dependence of the vibrational frequencies on coverage. In particular, the NO₂ stretching mode is sensitive to the charge transfer between the molecule and surface (cf. Table II) and hence on surface coverage. The theory predicts a considerable down-shift of 46 cm⁻¹ in the peak position of the NO₂ stretch when going from high ($\sqrt{3} \times \sqrt{3}$) to lowest (3×3) surface coverage. Experimentally, however, we did not observe such a significant shift of the NO₂ stretching mode across different concentrations. This prompted us to conclude that a very low coverage scenario as in (3×3) is *not* formed under the employed experimental conditions and that the molecules tend to arrange themselves at some intermediate coverage. Local variations of the surface coverage have been reported from experiments on single-crystal Au surfaces in ultra-high vacuum.^{3,32} Even if our experiments are performed under different conditions, it therefore appears plausible that a coexistence of various local geometries is a general characteristic feature of 4-NTP films also encountered here.

C. Sum frequency spectroscopy

To gain further insight into the tilt, polarization-dependent vibrational sum-frequency (vSF) spectra were obtained. Not only the *ppp* polarization combination but also the *ssp* one was used. Figure 8 presents the obtained spectra of the symmetric stretch, r^+ , of 4-NTP at 1339 cm⁻¹. It is well established that in principle the ratio between signals obtained using two polarization combinations for one specific vibrational mode can be used to determine the tilt angle of the moiety to which the mode belongs.³³

The analysis proceeds in two steps: First, the experimental spectra are fit to a model that allows us to extract the line strength of the symmetrical NO₂ stretch vibration for the two polarization combinations. Second, a theoretical model is built that yields the polarization ratio as a continuous function of tilt angle. By comparing the measured and the modeled polarization ratios, the most probable tilt angle is obtained.

The spectra were fit using the following expression:^{34,35}

$$I^{SF}(\omega_{IR}) \propto \left| \chi_{NR}^{(2)} \right| e^{i\gamma} + \frac{A}{\omega_{IR} - \omega + i\Gamma} \right|^2, \quad (2)$$

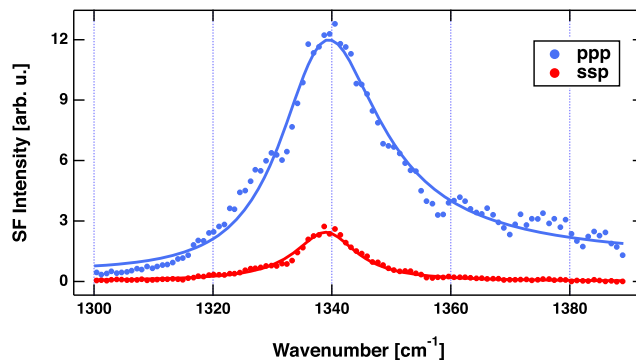


FIG. 8. SF spectra of the 4-NTP NO₂ symmetric stretch, r^+ . The band was observed utilizing the *ppp* and *ssp* polarization combinations. The solid lines represent fits to the data.

where $\chi_{NR}^{(2)}$ is the non-linear susceptibility of the non-resonant background. A , ω , and Γ are the vSF line strength, the position, and the width (HWHM) of the vibrational band, respectively. These parameters are real numbers, and A is positive in our model. ω_{IR} is the frequency of the incident IR light. Generally, Au substrates cause a strong non-resonant background due to the $d \rightarrow s$ interband transition at 480 nm. However, this background is relatively weak at IR wavenumbers of 1339 cm⁻¹ and 532 nm upconversion light when compared to the situation in the CH stretch region around 3000 cm⁻¹ but nevertheless cannot be ignored when fitting the data as is obvious from the asymmetrical line shape of the feature observed. From fitting the spectra, we obtained the line strength for the two polarization cases. They exhibit a ratio, A_{ssp}/A_{ppp} , of $1:4 \pm 0.02$. The results from fitting to Eq. (2) are presented in Table IV.

We followed Wang *et al.*³³ to calculate the theoretical intensity ratio of two different polarization combinations. Group theoretical considerations reduce the number of necessary hyperpolarizability components, β_{ijk}^a , which can be calculated using the following expression:³³

$$\beta_{i'j'k'}^a = -\frac{1}{2\epsilon_0\omega_q} \frac{\partial \alpha_{i'j'}}{\partial Q_q} \frac{\partial \mu_{k'}}{\partial Q_q}, \quad (3)$$

TABLE IV. Compilation of fit results. In the last line, the first three values are outside the plausible physical range; only the fourth ratio, IV/II, is considered further and plotted in Fig. 9.

	Fit no.	$\chi_{NR}^{(2)}$ (arb. u.)	γ (rad)	A_i (arb. u.)	ω_i (cm ⁻¹)	Γ_i (cm ⁻¹)
<i>ppp</i>	I	0.920 ± 0.129	-0.859 ± 0.137	27.37 ± 2.91	1338	10.21 ± 0.71
<i>ppp</i>	II	0.920 ± 0.129	1.146 ± 0.104	43.38 ± 1.86	1338	10.21 ± 0.71
<i>ssp</i>	III	0.120 ± 0.091	-1.705 ± 0.009	9.12 ± 0.84	1339	6.3 ± 0.3
<i>ssp</i>	IV	0.120 ± 0.091	1.685 ± 0.224	10.61 ± 0.43	1339	6.3 ± 0.3
$\chi_{ssp}^{(2)R,eff} / \chi_{ppp}^{(2)R,eff}$						
		III I	IV I	III II	IV II	
		0.292	0.395	0.116	0.157	

where $\tilde{\alpha}_{ij}^q := \partial\alpha_{ij}/\partial Q_q$ and $\partial\mu_{ij}/\partial Q_q$ are the first derivatives of the polarizability and of the dipole moment, respectively, along the normal coordinate of mode q . The non-zero susceptibility components are then calculated by averaging over the ring twist angle, ξ , and the azimuthal angle, ϕ , using a fixed tilt angle, θ (see Fig. 1 for details), according to the following equations:³³

$$\begin{aligned}\chi_{xxz}^{(2)} = \chi_{yyz}^{(2)} &= \frac{1}{4}N_s(\beta_{aac} + \beta_{bbc} + 2\beta_{ccc})(\cos\theta) \\ &\quad + \frac{1}{4}N_s(\beta_{aac} + \beta_{bbc} - 2\beta_{ccc})(\cos^3\theta), \\ \chi_{zxx}^{(2)} = \chi_{zxy}^{(2)} &= -\frac{1}{4}N_s(\beta_{aac} + \beta_{bbc} - 2\beta_{ccc})(\langle\cos\theta\rangle - \langle\cos^3\theta\rangle), \\ \chi_{zzz}^{(2)} &= \frac{1}{2}N_s(\beta_{aac} + \beta_{bbc})(\cos\theta) \\ &\quad - \frac{1}{2}N_s(\beta_{aac} + \beta_{bbc} - 2\beta_{ccc})(\cos^3\theta).\end{aligned}\quad (4)$$

Averaging over all possible azimuthal angles, ϕ , is rationalized by the laser spot sizes, which are orders of magnitude larger than the domains on the surface. The dependence on the twist angle, ξ , can safely be ignored as we find that adjusting it results only in small changes in the intensity ratio, an observation that is consistent with the results from the work of Cecchet *et al.*⁹ Taking into account the incident angles of the laser beams, $\Omega^{SF/VIS/IR}$, and accounting for the local fields by using Fresnel factors, the theoretical intensity ratio can be calculated as

$$\begin{aligned}\left(\frac{\chi_{ssp}^{(2)R,eff}}{\chi_{ppp}^{(2)R,eff}}\right)^2 &= \left(\frac{|L_{ii}^{SF}L_{jj}^{VIS}L_{kk}^{IR}\sin(\Omega^{IR})\chi_{yyz}^{(2)}|}{|\sum_{ijk}L_{ii}^{SF}L_{jj}^{VIS}L_{kk}^{IR}O_{ijk}\chi_{ijk}^{(2)}|}\right)^2 \\ &= \left(\frac{|A_{ssp}/i\Gamma_{ssp}|}{|A_{ppp}/i\Gamma_{ppp}|}\right)^2.\end{aligned}\quad (5)$$

$L_{ii}^{SF/VIS/IR}$ are Fresnel factor components for a particular direction i , j , or k in the laboratory coordinate system and the SF, vis, or IR beam, respectively. $\chi_{ijk}^{(2)}$ is one of the four independent tensor components of the second order susceptibility, namely, $\chi_{zzz}^{(2)}$, $\chi_{zxx}^{(2)}$, $\chi_{zxy}^{(2)}$, or $\chi_{xxx}^{(2)}$. We used the abbreviation $O_{ijk} = M_i(\Omega^{SF})M_j(\Omega^{VIS})M_k(\Omega^{IR})$, with $M_{i/j/k}(\Omega^{SF,VIS,IR})$ being either $\cos\Omega$ or $\sin\Omega$ depending on i , j , or k being either x or z . This ratio depends via the $\chi_{ijk}^{(2)}$ values on the molecular tilt angle, θ . Hence, the latter can be inferred as the theoretical ratio that has to match the experimental one.

We used the indices of refraction obtained by Ciesielski *et al.*³⁶ for a 35 nm Au film deposited on a glass slide to calculate the Fresnel factor components and a value of 1.62 for the refractive index of the monolayer as determined by Jakubowicz *et al.*³⁷ If Eq. (3) holds, then all of the necessary susceptibility components are linearly dependent on $\partial\mu_c/\partial Q_q$ so that only the molecular Raman tensor components need to be calculated in order to determine the theoretical SF intensity ratio. The molecular Raman tensor components were calculated by us for a free 4-NTP molecule and one adsorbed on a Au₁₉ cluster using the geometries (see Fig. 6) and methods described before (Sec. II), and the results are summarized in Table V. The ONO bond angle was calculated to be 123°. The intensity ratio given by Eq. (5) is

TABLE V. Calculated molecular Raman tensor components $\tilde{\alpha}_{ij}^q = \partial\alpha_{ij}/\partial Q_q$ of the free molecule and the molecule adsorbed on a Au₁₉ cluster for the NO₂ symmetric stretching mode.

	$\tilde{\alpha}_{aa}$ ($\text{\AA}^2\text{u}^{-0.5}$)	$\tilde{\alpha}_{bb}$ ($\text{\AA}^2\text{u}^{-0.5}$)	$\tilde{\alpha}_{cc}$ ($\text{\AA}^2\text{u}^{-0.5}$)
Free molecule	0.56	-0.04	7.59
On Au ₁₉ cluster	1.70	1.10	8.59

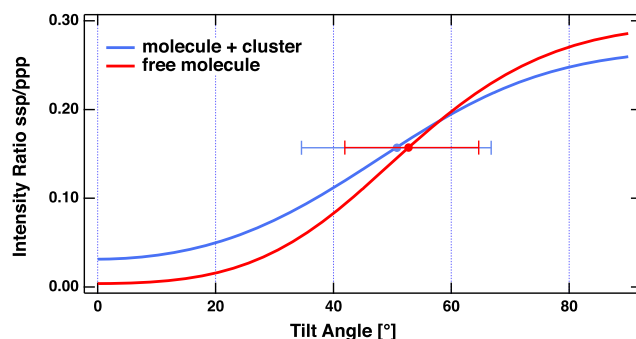


FIG. 9. The solid line represents the expected ratio between the line strength of the NO₂r⁺ mode when using the ssp or ppp polarization combination as a function of tilt angle with respect to the surface normal. The data points mark the result of our data analysis for the tilt angle with the error bar indicating the 95% confidence interval arising from the standard deviation of the fitting parameters. The blue and red theoretical modeling curves were obtained using the Raman tensor components calculated for 4-NTP on a Au₁₉ cluster and the free molecule, respectively.

evaluated as a continuous function of tilt angle θ , yielding a calibration curve as displayed in Fig. 9. It is worth mentioning that a normal distribution around a given tilt angle with a standard deviation of 10° was assumed, whereby the distribution was cut off at $\theta = 90^\circ$. The ratio of the line strength to the linewidth obtained from fitting the spectrum in the ssp polarization combination is then compared to those parameters obtained from fitting the spectrum taken in the ppp polarization combination, and the intersection of their quotient with the calibration curve allows us to extract the tilt angle. It has to be mentioned that the fitting (cf. Table IV) yields two sets for A and Γ for each polarization combination. This results in four possible intensity ratios. However, only one of these is to be considered further given the range of physically meaningful intensity ratios covered by the calibration curve (Fig. 9). Moreover, it is commonly reported that the relative phase γ has a value close to $\pi/2$.^{38–40} This is only the case for one pair, namely, II and IV in Table IV. From the ratio of 0.157, tilt angles of 53° and 51° are derived using the Raman tensor components of either the free molecule or the molecule attached to the Au cluster.

IV. CONCLUSIONS

The adsorption geometry of 4-nitrothiophenol has been investigated both theoretically by means of DFT calculations and experimentally by Raman spectroscopy and vSFS. The calculations show that the adsorption geometry of the thiophenols is governed by a

complex interplay of covalent bonding and electrostatic and dispersive interactions. These interactions attract the molecules to the surface, resulting in a tilted geometry with a tilt angle limited by the steric repulsion between neighboring molecules at larger coverage. In conclusion, the tilt angle obtained from analyzing the vSF spectra (50°) agrees best with the calculated value (53°) for a coverage of $1/4$ corresponding to a (2×2) structure. The previously reported⁹ somewhat larger tilt angle of 60° could be due to a slightly smaller coverage present at the preparation conditions of that study.

Unfortunately, it is not possible to determine the coverage from our vibrational spectroscopic data (vSFS and Raman). However, the Raman study suggests for samples incubated with a solution of smaller concentration that the molecules are adsorbed in an inclined geometry. At presumably larger surface coverages, a coexistence with molecules in a more upright geometry is observed. Let aside the systematic underestimation of the vibrational frequency of the NO_2 stretch by the PBE functional, the visible trend toward lower values with decreasing coverage appears as a valuable indicator to estimate the coverage. On that basis, our spectra also suggest a lower limit for the coverage, indicating that the structure should be denser than (3×3) . In line with older studies,¹ the calculations suggest that, in contrast to simple thiophenols, polyaromatic molecules will have a stronger tendency to form large domain SAMs due to the larger vdW interaction than what can be expected for thiophenol. In view of the present calculations, it is not anymore surprising that earlier proximity probe studies^{3,32} report that mono-phenylthiol molecules do not assemble in large domains of $(\sqrt{3} \times \sqrt{3})$ structure, highlighting that the latter should not be assumed to be the canonical structure for thiol self-assembly on Au(111) as is at times rashly inferred from studies of long-chain alkylthiol SAMs on Au(111).

SUPPLEMENTARY MATERIAL

The [supplementary material](#) contains further information about the adsorption geometries of 4-NTP, 4-NPTPT, and 4-NBPT (bonding and internal angles). It additionally contains numerical values of the adsorption energies for the $(\sqrt{3} \times \sqrt{3})$, (2×2) , and (3×3) surface unit cells for 4-NTP, 4-NPTPT, and 4-NBPT and for all types of vdW methods used.

ACKNOWLEDGMENTS

We acknowledge funding from the Deutsche Forschungsgemeinschaft (DFG, German Research Foundation) (Project No. 278162697) within the CRC 1242 “Non-Equilibrium Dynamics of Condensed Matter in the Time-Domain.”

DATA AVAILABILITY

The data that support the findings of this study are available within the article and its [supplementary material](#). Additional data that support the findings of this study are available from the corresponding author upon reasonable request.

REFERENCES

- 1 A.-A. Dhirani, R. W. Zehner, R. P. Hsung, P. Guyot-Sionnest, and L. R. Sita, “Self-assembly of conjugated molecular rods: A high-resolution STM study,” *J. Am. Chem. Soc.* **118**, 3319–3320 (1996).
- 2 W. Azzam, A. Al-Rashdi, A. Subaihi, M. Rohwerder, M. Zharnikov, and A. Bashir, “Annealing effect for self-assembled monolayers formed from terphenylethanethiol on Au(111),” *Phys. Chem. Chem. Phys.* **22**, 13580–13591 (2020).
- 3 S. Frey, V. Stadler, K. Heister, W. Eck, M. Zharnikov, M. Grunze, B. Zeysing, and A. Terfort, “Structure of thioaromatic self-assembled monolayers on gold and silver,” *Langmuir* **17**, 2408–2415 (2001).
- 4 C. M. Whelan, C. J. Barnes, C. G. H. Walker, and N. M. D. Brown, “Benzenethiol adsorption on Au(111) studied by synchrotron ARUPS, HREELS and XPS,” *Surf. Sci.* **425**, 195 (1999).
- 5 Y.-T. Tao, C.-C. Wu, J.-Y. Eu, W.-L. Lin, K.-C. Wu, and C.-H. Chen, “Structure evolution of aromatic-derivatized thiol monolayers on evaporated gold,” *Langmuir* **13**, 4018–4023 (1997).
- 6 H. McNally, D. B. Janes, B. Kasibhatla, and C. P. Kubiak, “Electrostatic investigation into the bonding of poly(phenylene) thiols to gold,” *Superlattices Microstruct.* **31**, 239–245 (2002).
- 7 L.-J. Wan, M. Terashima, H. Noda, and M. Osawa, “Molecular orientation and ordered structure of benzenethiol adsorbed on gold(111),” *J. Phys. Chem. B* **104**, 3563–3569 (2000).
- 8 K. T. Carron and L. Gayle Hurley, “Axial and azimuthal angle determination with surface-enhanced Raman spectroscopy: Thiophenol on copper, silver, and gold metal surfaces,” *J. Phys. Chem.* **95**, 9979–9984 (1991).
- 9 F. Cecchet, D. Lis, J. Guthmuller, B. Champagne, Y. Caudano, C. Silien, A. Addin Mani, P. A. Thiry, and A. Peremans, “Orientational analysis of dodecanethiol and *p*-nitrothiophenol SAMs on metals with polarisation-dependent SFG spectroscopy,” *ChemPhysChem* **11**, 607–615 (2010).
- 10 M. Linke, M. Hille, M. Lackner, L. Schumacher, S. Schlücker, and E. Hasselbrink, “Plasmonic effects of Au nanoparticles on the vibrational sum frequency spectrum of 4-nitrothiophenol,” *J. Phys. Chem. C* **123**, 24234 (2019).
- 11 C. M. Whelan, M. R. Smyth, and C. J. Barnes, “HREELS, XPS, and electrochemical study of benzenethiol adsorption on Au(111),” *Langmuir* **15**, 116–126 (1999).
- 12 F. Cecchet, D. Lis, J. Guthmuller, B. Champagne, G. Fonder, Z. Mekhalif, Y. Caudano, A. A. Mani, P. A. Thiry, and A. Peremans, “Theoretical calculations and experimental measurements of the vibrational response of *p*-NTP SAMs: An orientational analysis,” *J. Phys. Chem. C* **114**, 4106–4113 (2010).
- 13 O. Alexiadis, V. A. Harmandaris, V. G. Mavrantzas, and L. D. Site, “Atomistic simulation of alkanethiol self-assembled monolayers on different metal surfaces via a quantum, first-principles parametrization of the sulfur-metal interaction,” *J. Phys. Chem. C* **111**, 6380–6391 (2007).
- 14 E. Mete, M. Yortanlı, and M. F. Danişman, “A van der Waals DFT study of chain length dependence of alkanethiol adsorption on Au(111): Physisorption vs. chemisorption,” *Phys. Chem. Chem. Phys.* **19**, 13756–13766 (2017).
- 15 V. Blum, R. Gehrke, F. Hanke, P. Havu, V. Havu, X. Ren, K. Reuter, and M. Scheffler, “*Ab initio* molecular simulations with numeric atom-centered orbitals,” *Comput. Phys. Commun.* **180**, 2175–2196 (2009).
- 16 J. P. Perdew, K. Burke, and M. Ernzerhof, “Generalized gradient approximation made simple,” *Phys. Rev. Lett.* **77**, 3865–3868 (1996).
- 17 A. Tkatchenko and M. Scheffler, “Accurate molecular van der Waals interactions from ground-state electron density and free-atom reference data,” *Phys. Rev. Lett.* **102**, 073005 (2009).
- 18 A. Tkatchenko, A. Ambrosetti, and R. A. DiStasio, “Interatomic methods for the dispersion energy derived from the adiabatic connection fluctuation-dissipation theorem,” *J. Chem. Phys.* **138**, 074106 (2013).
- 19 A. Tkatchenko, R. A. DiStasio, R. Car, and M. Scheffler, “Accurate and efficient method for many-body van der Waals interactions,” *Phys. Rev. Lett.* **108**, 236402 (2012).
- 20 A. Ambrosetti, A. M. Reilly, R. A. DiStasio, and A. Tkatchenko, “Long-range correlation energy calculated from coupled atomic response functions,” *J. Chem. Phys.* **140**, 18A508 (2014).

- ²¹J. Hermann and A. Tkatchenko, "Density functional model for van der Waals interactions: Unifying many-body atomic approaches with nonlocal functionals," *Phys. Rev. Lett.* **124**, 146401 (2020).
- ²²J. Hermann (2021). "Libmbd," Zenodo. <https://doi.org/10.5281/zenodo.594879>.
- ²³J. M. Morbec and P. Kratzer, "The role of van der Waals interactions in the adsorption of anthracene and pentacene on the Ag(111) surface," *J. Chem. Phys.* **146**, 034702 (2017).
- ²⁴B. P. Klein, J. M. Morbec, M. Franke, K. K. Greulich, M. Sachs, S. Parhizkar, F. C. Bocquet, M. Schmid, S. J. Hall, R. J. Maurer, B. Meyer, R. Tonner, C. Kumpf, P. Kratzer, and J. M. Gottfried, "Molecule-metal bond of alternant versus nonalternant aromatic systems on coinage metal surfaces: Naphthalene versus azulene on Ag(111) and Cu(111)," *J. Phys. Chem. C* **123**, 29219–29230 (2019).
- ²⁵S. R. Kachel, B. P. Klein, J. M. Morbec, M. Schöniger, M. Hutter, M. Schmid, P. Kratzer, B. Meyer, R. Tonner, and J. M. Gottfried, "Chemisorption and physisorption at the metal/organic interface: Bond energies of naphthalene and azulene on coinage metal surfaces," *J. Phys. Chem. C* **124**, 8257–8268 (2020).
- ²⁶A. Maeland and T. B. Flanagan, "Lattice spacings of gold-palladium alloys," *Can. J. Phys.* **42**, 2364–2366 (1964).
- ²⁷L. Bengtsson, "Dipole correction for surface supercell calculations," *Phys. Rev. B* **59**, 12301–12304 (1999).
- ²⁸E. van Lenthe, E. J. Baerends, and J. G. Snijders, "Relativistic total energy using regular approximations," *J. Chem. Phys.* **101**, 9783–9792 (1994).
- ²⁹J. Neugebauer, M. Reiher, C. Kind, and B. A. Hess, "Quantum chemical calculation of vibrational spectra of large molecules—Raman and IR spectra for buckminsterfullerene," *J. Comput. Chem.* **23**, 895–910 (2002).
- ³⁰H. Shang, N. Raimbault, P. Rinke, M. Scheffler, M. Rossi, and C. Carbogno, "All-electron, real-space perturbation theory for homogeneous electric fields: Theory, implementation, and application within DFT," *New J. Phys.* **20**, 073040 (2018).
- ³¹S. Schlücker, "Surface-enhanced Raman spectroscopy: Concepts and chemical applications," *Angew. Chem., Int. Ed.* **53**, 4756–4795 (2014).
- ³²J. U. Nielsen, M. J. Esplandiú, and D. M. Kolb, "4-nitrothiophenol SAM on Au(111) investigated by in situ STM, electrochemistry, and XPS," *Langmuir* **17**, 3454–3459 (2001).
- ³³H.-F. Wang, W. Gan, R. Lu, Y. Rao, and B.-H. Wu, "Quantitative spectral and orientational analysis in surface sum frequency generation vibrational spectroscopy (SFG-VS)," *Int. Rev. Phys. Chem.* **24**, 191 (2005).
- ³⁴M. Buck and M. Himmelhaus, "Vibrational spectroscopy of interfaces by infrared-visible sum frequency generation," *J. Vac. Sci. Technol. A* **19**, 2717 (2001).
- ³⁵F. Vidal and A. Tadjeddine, "Sum-frequency generation spectroscopy of interfaces," *Rep. Prog. Phys.* **68**, 1095 (2005).
- ³⁶A. Ciesielski, L. Skowronski, M. Trzcinski, E. Górecka, P. Trautman, and T. Szoplik, "Evidence of germanium segregation in gold thin films," *Surf. Sci.* **674**, 73–78 (2018).
- ³⁷A. Jakubowicz, H. Jia, R. M. Wallace, and B. E. Gnade, "Adsorption kinetics of *p*-nitrobenzenethiol self-assembled monolayers on a gold surface," *Langmuir* **21**, 950–955 (2005).
- ³⁸A. G. Lambert, P. B. Davies, and D. J. Neivandt, "Implementing the theory of sum frequency generation vibrational spectroscopy: A tutorial review," *Appl. Spectrosc. Rev.* **40**, 103–145 (2005).
- ³⁹C. C. Rich, K. A. Lindberg, and A. T. Krummel, "Phase acrobatics: The influence of excitonic resonance and gold nonresonant background on heterodyne-detected vibrational sum frequency generation emission," *J. Phys. Chem. Lett.* **8**, 1331–1337 (2017).
- ⁴⁰P. A. Covert and D. K. Hore, "Assessing the gold standard: The complex vibrational nonlinear susceptibility of metals," *J. Phys. Chem. C* **119**, 271–276 (2014).